





Dissecting the Interstellar Media of A Wolf-Rayet Galaxy at $z = 2.76$

TAKAHIRO MORISHITA ¹, MASSIMO STIAVELLI ², STEFAN SCHULDT ^{3,4} AND CLAUDIO GRILLO ^{3,4}

¹*IPAC, California Institute of Technology, MC 314-6, 1200 E. California Boulevard, Pasadena, CA 91125, USA*

²*Space Telescope Science Institute, 3700 San Martin Drive, Baltimore, MD 21218, USA*

³*Dipartimento di Fisica, Università degli Studi di Milano, Via Celoria 16, I-20133 Milano, Italy*

⁴*INAF - IASF Milano, via A. Corti 12, I-20133 Milano, Italy*

(Accepted November 1, 2024)

Submitted to ApJ

ABSTRACT

We report JWST/NIRSpec observations of a star-forming galaxy at $z = 2.76$, MACSJ1149-WR1. We securely detect two temperature-sensitive auroral lines, [S III] 6312 (7.4σ) and [O II] 7320+7331 doublets (10σ), and tentatively [N II] 5755 (2.3σ) for the first time in an individual galaxy at $z > 1$. We perform a detailed analysis of its interstellar media (ISM), and derive electron temperatures, various heavy element abundances (O/H, N/O, S/O, and Ar/O) in the hot ionized region, and the neutral fraction in the warm ionized region. MACSJ1149-WR1 shows a broad feature at the wavelength of He II 4686, which consists of a broad (~ 1000 km/s), blue-shifted (~ -110 km/s) line component. Taken together with its mildly elevated N/O abundance, we conclude that MACSJ1149-WR1 is experiencing a young starburst ($\lesssim 10$ Myr), likely hosting a large number of Wolf-Rayet stars. None of its spectral features support the presence of AGN, including: (i) the absence of broad components and velocity shifts in Hydrogen recombination lines, (ii) low [Fe II]1.257 $\mu\text{m}/\text{Pa}\beta$ ratio, and (iii) the absence of high-ionization lines. Our analysis using He I lines reveals a higher electron temperature and a higher attenuation value, indicating that He I may probe a smaller spatial scale than H I, presumably the region dominated by the aforementioned Wolf-Rayet stars. The star formation rates derived from various He I lines broadly agree with those from Hydrogen recombination lines. We thus advocate that He I can be an excellent, independent probe of multi-phase ISM in the era of JWST.

1. INTRODUCTION

The gas cycle within galaxy systems is fundamental to their formation processes. The interstellar medium (ISM) undergoes continuous chemical enrichment through the infusion of ejecta from previous generations of stars, while simultaneously being diluted by relatively pristine gas infalling from surrounding circumgalactic resources. The accumulation of stars formed through this complex interplay of gas reservoirs shapes the major structures of galaxies observed in later epochs (e.g., Lilly et al. 2013; Anglés-Alcázar et al. 2017). Therefore, it is crucial to observationally constrain the properties of the ISM in galaxies during their active formation epochs.

The two most important quantities characterizing ISM are the electron temperature (T_e) and electron density (n_e). These properties not only define the basic nature of ISM but also play a crucial role in determining other properties, such as heavy element abundances. Traditionally, the former has been determined by using an optical auroral line sensitive to temperature, such as [O III] 4363, whereas the latter is derived from the ratio of doublet lines, such as [S III] 6716+6731 and [O II] 3726+3729 (e.g., Osterbrock & Ferland 2006, Izotov et al. 2006 for a detailed analysis).

Previously, accessing auroral lines in galaxies at $z > 1$ posed a significant challenge due to their faintness compared to the bright emission lines of the same species (e.g., [O III] 4363/[O III] 5007 $\sim 1/100$). Despite a few exceptional cases (Sanders et al. 2016, 2020; Gburek et al. 2019), these lines have generally remained elusive. However, with the advent of the James Webb

Space Telescope (JWST), this situation has changed dramatically. Multiple sources have now been identified with significant [O III] 4363 detection, up to redshift of $z = 9.5$ (Arellano-Córdova et al. 2022; Schaerer et al. 2022; Nakajima et al. 2023; Sanders et al. 2023a; Curti et al. 2023; Laseter et al. 2023; Morishita et al. 2024). Additionally, in some instances, auroral lines other than [O III] 4363 have been observed. For example, Sanders et al. (2023c) reported the detection of [O II] 7320+7331 (4.4σ) in two galaxies at $z = 2.18$. Later, Rogers et al. (2023) reported the same doublet lines, along with another auroral line [S III] 6312 detected at 9σ in Q2343-D40, a galaxy at $z = 2.96$. Strom et al. (2023) showcases a number of faint lines in composite spectrum of galaxies at $z = 1-3$, including the auroral [N II] 5755 line.

In the literature, it has been common practice to use a single temperature to infer multiple element abundances. However, this approach is only valid under certain conditions, namely when emission lines of different species coincide in the roughly same, uniform ionization structure. This assumption often proves inaccurate, particularly at high redshifts due to a number of mergers and other dynamically violent processes (e.g., Tacconi et al. 2010; Genzel et al. 2011). Given the capability of JWST enabling multiple auroral line detections for individual systems, ISM studies stand to benefit significantly from more detailed analysis.

In this paper, we report the detection of three auroral lines in a galaxy at $z = 2.76$, enabling us to compare electron temperatures derived for different elements. Our deep JWST/NIRSpec spectrum captures 31 emission lines spanning the rest-frame range of $0.45-1.3\mu\text{m}$ (Fig. 1), facilitating a comprehensive analysis of its ISM properties. Notably, our spectrum also reveals a broad line complex at the wavelength of He II 4686, a characteristic feature of Wolf-Rayet stars.

This paper is structured as follows: In Sec. 2, we present our observations and their reduction. In Sec. 3, we perform a spectroscopic analysis, followed by a photometric analysis of the host galaxy in Sec. 4. In Sec. 5.1, we discuss the inferred element abundances in the context of massive stars. In Sec. 5.2, we infer the absence of AGN using multiple emission line diagnostics. In Sec. 5.3, we attempt to infer the ISM properties by using a series of He I lines detected across the wavelength range, as an independent probe of ISM. Where relevant, we adopt the AB magnitude system (Oke & Gunn 1983; Fukugita et al. 1996), cosmological parameters of $\Omega_m = 0.3$, $\Omega_\Lambda = 0.7$, $H_0 = 70\text{ km s}^{-1}\text{ Mpc}^{-1}$, and the Chabrier (2003) initial mass function.

For convenience, we express flux ratios as follows:

$$R_3 = \log([[\text{O III}] 4959 + [\text{O III}] 5007]/\text{H}\beta)$$

$$R_{2,7325} = \log([[\text{O II}] 7320 + [\text{O II}] 7331]/\text{H}\beta)$$

$$R_{S2} = \log([[\text{S II}] 6716 + [\text{S II}] 6731]/\text{H}\beta)$$

$$R_{S3} = \log([\text{S III}] 6312/\text{H}\beta)$$

$$R_{Ar3} = \log([\text{Ar III}] 7135/\text{H}\beta)$$

$$R_{N2} = \log([[\text{N II}] 6548 + [\text{N II}] 6584]/\text{H}\beta).$$

2. JWST/NIRSPEC AND NIRCAM OBSERVATIONS

We briefly describe our JWST/NIRSpec and NIRCAM observations, conducted as part of the GTO1199 program, targetted on the field of the galaxy cluster MACS J1149.6+2223 ($z = 0.54$; Stiavelli et al. 2023). Readers are referred to Morishita et al. (2024) for the full details about our observations and data reduction.

Our target galaxy in this paper, MACSJ1149-WR1, was observed for 9.2 hrs (excluding overhead), with each of the G235M and G395M gratings, under the NIRSpec Multi-Object Spectroscopy (MSA) mode. We reduced the MSA data using *msaexp*¹ (ver. 0.8.5), by following Morishita et al. (2023). The one-dimensional spectrum was extracted via optimal extraction.

We followed the same steps for JWST/NIRCam imaging reduction and photometry as presented in Morishita & Stiavelli (2023). We identified sources in the detection image using SExtractor (Bertin & Arnouts 1996), and measured their fluxes on the psf-matched mosaic images with a fixed aperture of radius $r = 0.''16$. MACSJ1149-WR1 is located in an area relatively free from contamination by surrounding sources and foreground cluster galaxies, assuring a robust flux estimate. The magnification by the foreground cluster is estimated to be $\mu = 1.34^{+0.02}_{-0.01}$ (Schuldt et al., in prep.). While the magnification factor is not as significant as for sources near the cluster center, we note that this effectively increases the on-source exposure time by a factor of $\mu^2 \sim 1.8$, thereby significantly improving S/Ns.

3. ISM ANALYSIS

In what follows, we describe our analysis of the ISM using the extracted 1d spectrum.

3.1. Emission Line Measurement

We model each emission line of interest with a Gaussian function. Our basic strategy is to define a wavelength window for each line, model the underlying continuum spectrum by a 2nd-order polynomial fit, and subtract it from the 1-d spectrum before the Gaussian

¹ <https://github.com/gbrammer/msaexp>

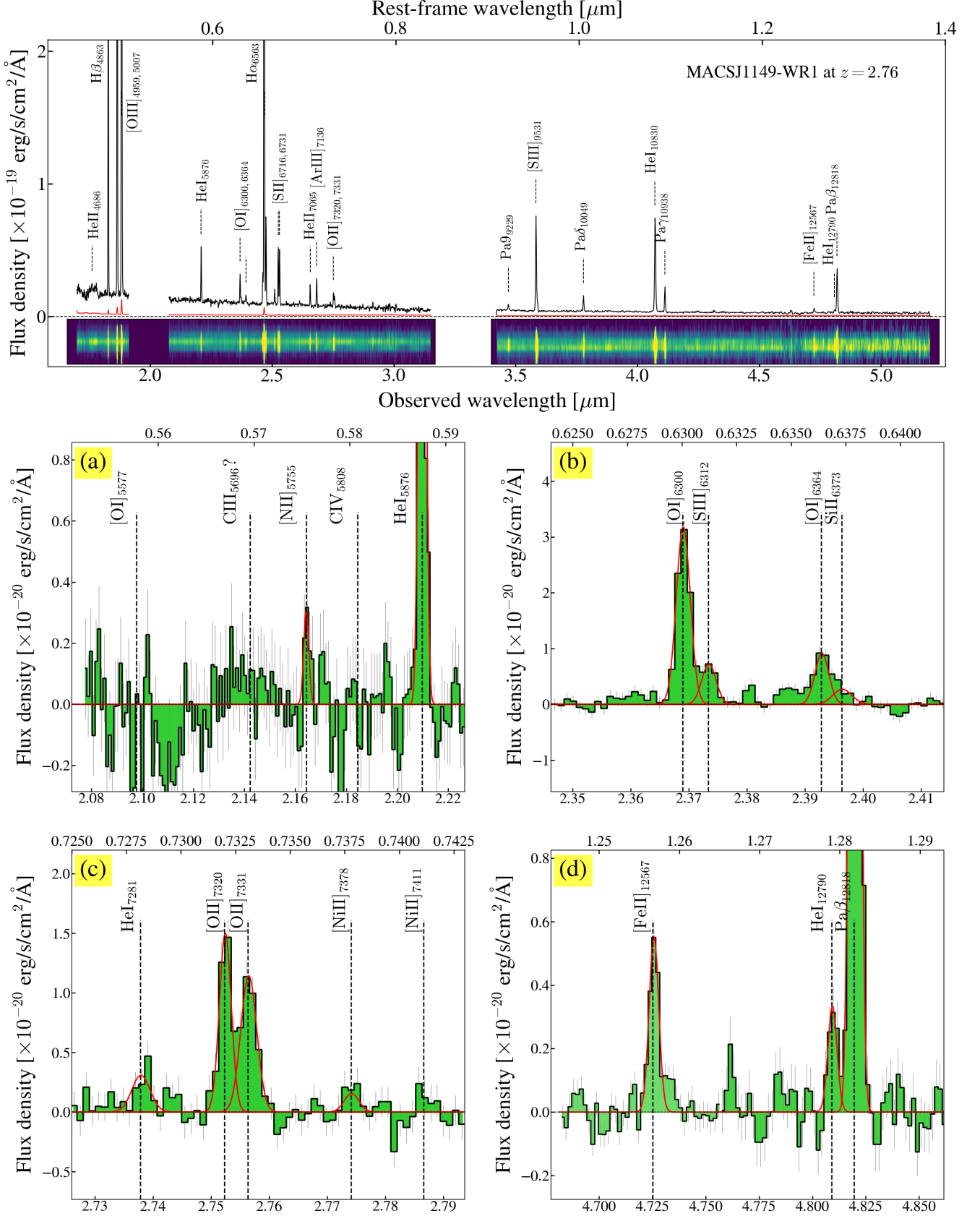


Figure 1. (Top): One-dimensional spectrum of MACSJ1149-WR1. Bright lines are labelled. The noise level is also shown (red line). Two-dimensional spectrum is shown at the bottom of the panel (G235M and G395M). The gap within the G235M spectrum is caused by a detector gap. (Bottom): Zoom-in plot of the continuum-subtracted spectrum around faint emission lines: (a) [N II] 5755, (b) [S III] 6312, (c) [O II] 7320+7331, and (d) [Fe II] 1.257 μm . The fitted gaussian for each detected line is shown (red lines). The location of C IV 5808, a characteristic line of WR stars, and [O I] 5755, another auroral line, are indicated despite being undetected. For the He II 4686 line complex, see Fig. 2.

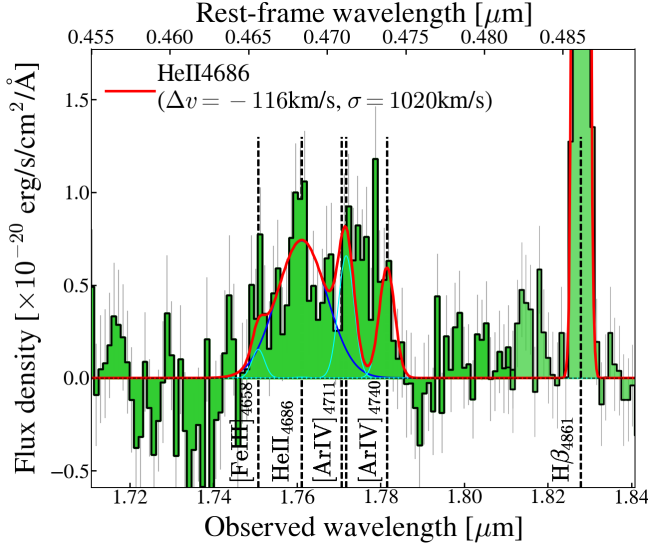


Figure 2. Zoom-in plot around the He II 4686 complex. The He II 4686 complex is fitted with multiple gaussian components: broad He II 4686 line (blue line) and narrow [Ar IV] 4711, 4740, and He I 4714 lines (thin cyan lines). The total model is shown in red. The He II line is broad ($\sigma \sim 1000$ km/s) and blue-shifted (~ -110 km/s) from the systemic redshift.

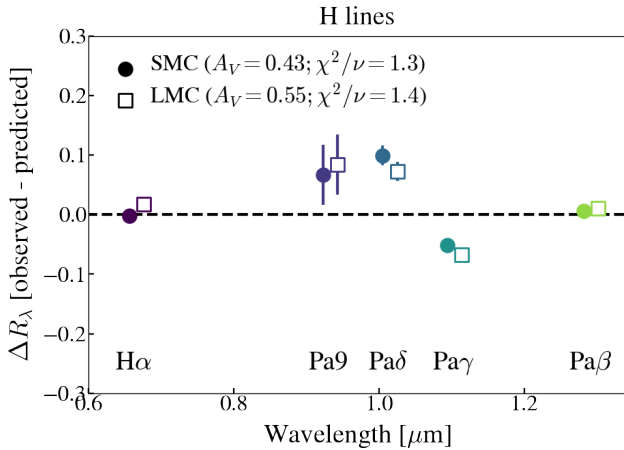


Figure 3. Residual of the line flux extinction correction, $\Delta R_\lambda = (I_\lambda / I_{\text{H}\beta})_{\text{measured}} - (I_\lambda / I_{\text{H}\beta})_{\text{model}}$, for various Hydrogen recombination lines. The results with the SMC (LMC) dust model are shown with filled circles (empty squares). For MACSJ1149-WR1, the SMC dust model provides a slightly better fitting result. H β is not shown, as the line is used as the pivotal wavelength (i.e. $\Delta R_\lambda = 0$).

fit is carried out. The model includes three parameters, amplitude, line width, and redshift. When multiple lines are located close to each other, we fit those simultaneously using a common redshift parameter, so blending can effectively be resolved. In addition, doublet lines

(i.e. [O III] $_{\lambda\lambda 4959+5007}$ and [N II] $_{\lambda\lambda 6550+6585}$) are modelled with a fixed line ratio (1:3 and 1:1.7, respectively), with single line width and redshift parameters. The total flux of the doublets estimated in this way remains robust, while we note that the ratio could have a systematic uncertainty for $\lesssim 10\%$ (e.g., Storey & Zeippen 2000). For doublet lines that we aim to measure the ratio (i.e. [O II] 7320,7331 and [S II] 6718,6733), we fit them without having such constraints.

The integrated flux of each line is estimated by summing the corresponding Gaussian component, and the flux error is estimated by summing the error weighted by the amplitude of the Gaussian model in quadrature. We then compare this flux error with the one originating in the model uncertainty and take the one larger for each line. By having these two uncertainty estimates, the final flux error is conservative and accurate in potential anomalous occasions, e.g., when one of the doublet lines fall on a detector gap. In the following analysis, we adopt flux measurements when the line is detected (signal-to-noise ratio $S/N \geq 2$); for those not detected, we adopt $2\text{-}\sigma$ flux upper limits. We detect 31 lines at $S/N > 2$. We report emission line fluxes estimated in Table 1.

3.1.1. Faint Auroral Lines

We detect auroral emission lines, [S III] 6312 and [O II] 7320,7331 at a significant confidence level (7.1σ , 10.8σ , 9.3σ , respectively), and tentatively [N II] 5755 line (2.4σ ; Panels (a)–(c) in Fig. 1). The [N II] line was successfully fit with a Gaussian but the resulting width was found to be narrower than the resolution limit. As such, we fix the line width to the one defined by spectral resolution at the corresponding wavelength ($R \sim 910$, or ~ 140 km/s), making its flux estimate conservative. We note that widths of other lines are also found similarly narrow, which supports our procedure on [N II] here.

These lines are used to infer the electron temperature (Sec. 3.3), which is essential for robust inference of element abundances (Sec. 3.4). The ratio of the [O II] doublets is $I_{7320}/I_{7331} = 0.97 \pm 0.12$. While the [S III] 6312 line is located near [O I] 6300 and partially blended, the peak of the line is clearly separated and enables robust flux estimate.

3.1.2. Broad He II 4686 Line Complex

We find a broad feature at the wavelength of He II 4686 (Fig. 2). The feature is characteristic to galaxies dominated by Wolf-Rayet (WR) stars (e.g., Allen et al. 1976; Brinchmann et al. 2008), often referred to as blue bump. In addition to broad He II 4686, WR galaxies often show broad N III 4640 and C III 4650 emission lines, depending on the type of Wolf-Rayet stars (Carbon-dominated

WC or Nitrogen dominated WN) and their sub-classes (Smith 1968; van der Hucht 2001), as well as narrow lines such as [Fe III] 4658, [Ar IV] 4711, 4740, and He I 4714.

We attempt to fit the line complex with a multi-component gaussian model. After experimenting various combinations, we found that a simple model that consists of one broad component (corresponding to He II) and four narrow components ([Fe III], [Ar IV] doublets, He I) well reproduces the complex within reasonable parameter ranges. The redshift of all components is set to a single value during the fit, to avoid extra complexity.

With this configuration, we find that the broad He II component is characterized broad ($\sigma \sim 1000$ km/s) and blue-shifted for ~ -110 km/s from the systemic redshift. The derived line width is large but within the range of local WR galaxy samples (e.g., Brinchmann et al. 2008).

The blue bump spectral feature can be characterized by its flux ratio to, e.g., H β . We find this to be ~ 0.15 for MACSJ1149-WR1, which is consistent with the range found in local galaxies (e.g., ~ 0.1 – 1 ; Sargent & Filippenko 1991).

The addition of broad N III and/or C III component turned out unnecessary in our case. Those two lines fall near the blue edge of the observed emission feature. In fact, the model including those was found incompatible without introducing an unreasonably large velocity shift ($\gtrsim +2000$ km/s). We do not clearly see C III 5696 and C IV 5808 in our spectrum, i.e. another characteristic feature called “red bump,” though we notice there exists slight excess of flux at the corresponding wavelength (Fig. 1). As such, the absence of significant C III and C IV emission near the He II complex is not surprising.

Due to the sensitivity limitation in our spectrum, further characterization of the underlying WR stars should defer to a future study with additional data. Yet, our analysis has clearly characterized MACSJ1149-WR1 as a galaxy likely hosting a non-negligible number of WR stars (see also Sec 5.1).

3.1.3. Other Emission Lines

Besides the lines remarked in the previous two subsections, we note the detection of lines that underrepresent in ISM studies in the literature, including [Si II] 6373 (Fig. 1, panel b), [Fe II] 1.257 μ m (d), and a series of He I lines. While [Fe II] has a low ionization potential (7.9 eV), it is often seen in AGN or shock-dominated regions. This is because iron element is highly depleted on dust grains and the element is observable upon the destruction of dust grains. As such, a high [Fe II] line ratio (e.g., to Pa β) would indicate the presence of such mechanisms in act (see Sec. 5.2). For the same reason, [Fe II] is not

a good line for iron abundance estimate, as the fraction of iron atoms in the ISM over those depleted on dust grains is not easily observable.

Overall, all the detected lines are found to be narrow, with $\sigma \sim 100$ – 200 km/s, comparable to the instrumental resolution, except for those in the aforementioned He II line complex. Some Hydrogen recombination lines are detected at high significance, and yet we do not observe clear evidence of a broad component.

3.2. Dust Extinction

Extinction in ISM is estimated by using the detected Hydrogen recombination lines i.e. H β , H α , Pa9, Pa δ , Pa γ , and Pa β . The intrinsic emissivity of each line is estimated under the assumption of Case B, with $T = 10000$ K (Osterbrock & Ferland 2006). While the recombination coefficients have temperature dependence, we find in the following section that our assumption is reasonable. We estimate the attenuation, A_V , via chi-square minimization between the observed and the predicted line ratios in the base of H β , $R_\lambda = I_\lambda / I_{H\beta}$. Fig. 3 shows the comparison, where we find $A_V = 0.43$ for the SMC dust curve (Gordon et al. 2003) and $A_V = 0.55$ for the LMC curve (Calzetti et al. 2000). We find that the SMC model gives a slightly better fitting result ($\chi^2/\nu = 1.3$) over the LMC’s ($= 1.4$). As such, in the following analysis, we adopt the correction obtained with the SMC curve.

3.3. Electron Density and Temperature

Electron density can be estimated from doublet lines such as [O II] 3726, 3729 and [S II] 6718, 6733. However, electron density has a mild dependency on electron temperature, and vice versa. As such, it is desirable to determine both quantities simultaneously, e.g., through an iterative approach.

We first determine electron density and electron temperature using two line ratios, [S II] 6718/[S II] 6733 and [S III] (9531+9069)/[S III] 6312. For electron density, we use the formula presented in Sanders et al. (2020), with the temperature dependence as outlined in Osterbrock & Ferland (2006):

$$n_e = \frac{(c[S \text{ II}]_{6718}/[S \text{ II}]_{6733} - ab)}{(a - [S \text{ II}]_{6718}/[S \text{ II}]_{6733})} \left(\frac{T_e}{10^4}\right)^{-1/2}, \quad (1)$$

with $a = 0.4315$, $b = 2107$, and $c = 627.1$. For electron temperature, we use Eq. (5.7) in Osterbrock & Ferland (2006):

$$\frac{[S \text{ III}]_{9069} + [S \text{ III}]_{9531}}{[S \text{ III}]_{6312}} = \frac{5.44 \exp(2.28 \times 10^4/T_e)}{1 + 3.5 \times 10^{-4} n_e / T_e^{1/2}}, \quad (2)$$

where n_e and T_e hold the same values as in Eq. 1. Note that the [S III] 9096 line falls in the detector gap,

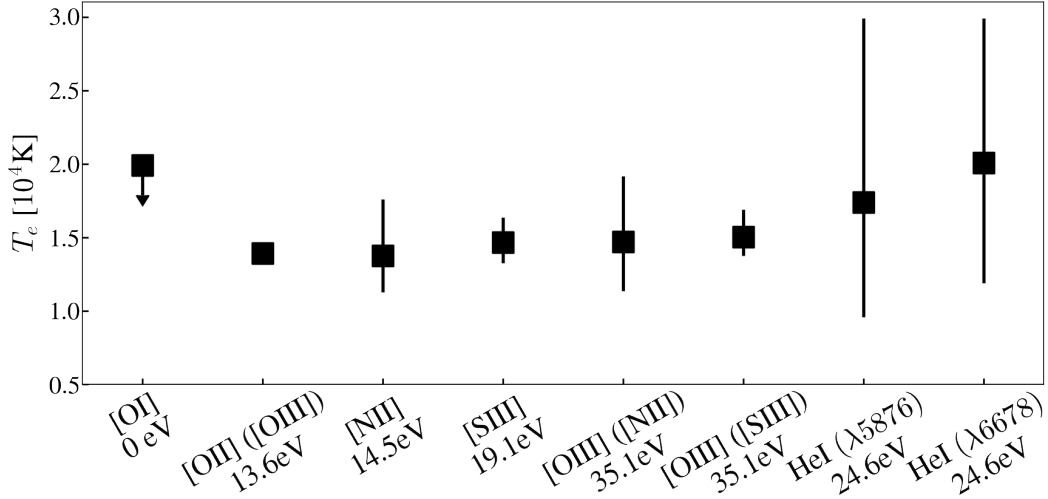


Figure 4. Electron temperatures of MACSJ1149-WR1 measured with various temperature sensitive lines (Sec. 3.3). Ionization potential is shown in the label of each line. [O III] ([S III]) is the temperature derived from $T_e([S III])$ (Eq. 4) and [O III] ([N II]) from $T_e([N II])$ (Eq. 5). $T_e([O I])$ is derived using the lower limit [O I] (6300+6364)/[O I] 5577, and thus the derived 1σ upper limit is shown. Two temperature measurements, $T_e(He I)$, derived using the line ratios He I 7281/He I 5876 and He I 7281/He I 6678, are shown (Sec. 5.3).

and thus we instead use a fixed ratio of the doublets, $I_{9531}/I_{9096} = 2.5$ (Sanders et al. 2020). By solving the two equations above simultaneously, we find $n_e([S II]) = 363^{+76}_{-64} \text{ cm}^{-3}$ and $T_e([S III]) = 1.47^{+0.17}_{-0.14} \text{ K}$. Our spectra do not have the wavelength coverage for the [O II] 3726,3729 doublets. The [O II] 7320,7331 doublet ratio has almost no dependency on n_e . Therefore, we adopt $n_e([S II])$ in the following analysis. Throughout the following analyses, we propagate the uncertainty of n_e , in addition to the uncertainties of flux measurements of interest.

Since our spectra do not cover the temperature sensitive [S II]_{4068,4076} lines (e.g., Shaw & Dufour 1995), we cannot directly obtain $T_e([S II])$. However, our iterative analysis above implicitly assumes $T_e([S II]) = T_e([S III])$, whereas in the local universe the former is found systematically lower (\sim a few 1000 K, e.g., Pérez-Montero 2017). (Also, see below where we derive the temperature from N^+ , which has a similar ionizing potential to S^+ .) However, we find the impact from this remains relatively small. For example, by setting $T_e([S II]) = T_e([S III]) - 2000$, we find $n_e = 338 \pm 47 \text{ cm}^{-3}$. The change in n_e has little impact in the following analyses. As such, we adopt the n_e measurement obtained with the $T_e([S II]) = T_e([S III])$ assumption in the following analysis.

With [N II] 5755, we use Eq. (5.5) in Osterbrock & Ferland (2006):

$$\frac{[N II]_{6548} + [N II]_{6583}}{[N II]_{5755}} = \frac{8.23 \exp(2.50 \times 10^4 / T_e)}{1 + 4.4 \times 10^{-3} n_e / T_e^{1/2}}, \quad (3)$$

and obtain $T_e([N II]) = 1.37^{+0.38}_{-0.25} \times 10^4 \text{ K}$. The larger error in the estimate here comes from the measurement uncertainty in the [N II] 5755 flux.

We then attempt to estimate the temperatures of [O II] and [O III], which are critical to oxygen abundance estimate. This is, however, tricky in our case, since our spectra do not cover the wavelength range of [O II] 3726,3729 nor [O III] 4363. As such, in the following analysis we assume $T_e([O II]) = T_e([N II])$, as the two lines have similar ionization potential (13.6 eV and 14.5 eV).

$T_e([O III])$ can be inferred from $T_e([S III])$, by using Eq.(15) in Izotov et al. (2006):

$$t_e([S III]) = -1.276 + t_e([O III])(2.645 - 0.546 t_e([O III])), \quad (4)$$

where t_e represents the corresponding temperature scaled by $1/10^4$. By solving the equation, we obtain $T_e([O III])_{[S III]} = 1.50^{+0.19}_{-0.13} \times 10^4 \text{ K}$.

Alternatively, one can estimate $T_e([O III])$ via $T_e([O II])$ by using Eq.(14) in Izotov et al. (2006):

$$t_e([O II]) = -0.744 + t_e([O III])(2.338 - 0.610 t_e([O III])). \quad (5)$$

This gives $T_e([O III])_{[N II]} = 1.47^{+0.45}_{-0.33} \times 10^4 \text{ K}$, which is consistent with $T_e([O III])_{[S III]}$ but has a larger uncertainty. We adopt $T_e([O III])_{[S III]}$ for the oxygen abundance inference in the following section.

As a sanity check, we derive $T_e([O II])$ via Eq. 5, by using $T_e([O III])_{[S III]}$. This gives $T_e([O II]) = 1.4 \pm 0.1 \times 10^4 \text{ K}$. The estimate is consistent with $T_e([N II])$, which

validates the assumption, $T_e([\text{O II}]) = T_e([\text{N II}])$, made above.

Lastly, with the lower limit flux ratio $[\text{O I}](6300+6364)/[\text{O I}](5577)$, we find $T_e([\text{O I}]) < 1.99 \times 10^4 \text{ K}$ (1σ).

For Ar^{2+} , while we detect $[\text{Ar III}](7135 \text{ and } 7751 \text{ lines})$, our spectrum do not have the wavelength coverage for $[\text{Ar III}](5192)$, due to the detector gap, which can be a good temperature indicator by combining with the doublet lines (e.g., Keenan et al. 1988; Proxauf et al. 2014). We thus adopt $T_e([\text{S III}])$ in the Ar^{2+} abundance inference below.

In Fig. 4, we compare the derived temperatures. Overall, they are in good agreement within the uncertainties. We do not see any significant trend in T_e with ionizing potential, indicating that their ionizing regions likely coincide.

3.4. Heavy Element Abundances

Now equipped with the electron density from $[\text{S II}]$ and electron temperature from multiple lines, we attempt to obtain heavy element abundances.

Oxygen abundance is estimated by deriving O^{2+}/H^+ and O^+/H^+ separately. Each abundance can be estimated by substituting the temperatures into the following two equations from Izotov et al. (2006):

$$12 + \log \text{O}^{2+}/\text{H}^+ = R_3 + 6.200 + 1.251/t_e([\text{O III}]) - 0.55 \log t_e([\text{O III}]) - 0.014 t_e([\text{O III}]), \quad (6)$$

$$12 + \log \text{O}^+/\text{H}^+ = R_{2,7325} + 6.901 + 2.487/t_e([\text{O II}]) - 0.483 \log t_e([\text{O II}]) - 0.013 t_e([\text{O II}]) + \log(1 - 3.48x), \quad (7)$$

where $x = 10^{-4} n_e t_e^{-0.5}$. We obtain $12 + \log \text{O}^{2+}/\text{H}^+ = 7.78_{-0.10}^{+0.08}$ and $12 + \log \text{O}^+/\text{H}^+ = 7.34_{-0.04}^{+0.04}$. The contribution from the atomic oxygen and triply ionized oxygen are considered negligible. As a sanity check, we run cloudy to calibrate $[\text{O III}](5007)/[\text{O III}](7320)$ to ionization parameter $\log U$. For the observed ratio, we find $\log U \sim -2.6$, where O^0 is expected to be $< 10\%$ and $\text{O}^{3+} \ll 1\%$ relative to the total oxygen abundance (e.g., Berg et al. 2019). As such, we adopt

$$\frac{\text{O}}{\text{H}} = \frac{\text{O}^+}{\text{H}^+} + \frac{\text{O}^{2+}}{\text{H}^+} \quad (8)$$

and obtain $12 + \log (\text{O}/\text{H}) = 7.92_{-0.08}^{+0.07}$.

We follow similar approaches for Sulfur and Nitrogen using the following equations from Izotov et al. (2006):

$$12 + \log \text{S}^+/\text{H}^+ = R_{S2} + 5.439 + 0.929/t_e([\text{S II}]) - 0.28 \log(t_e([\text{S II}])) - 0.018 t_e([\text{S II}]) + \log(1 + 1.39x), \quad (9)$$

$$12 + \log \text{S}^{2+}/\text{H}^+ = R_{S3} + 6.690 + 1.678/t_e([\text{S III}]) - 0.47 \log(t_e([\text{S III}])) - 0.010 t_e([\text{S III}]), \quad (10)$$

$$12 + \log \text{N}^+/\text{H}^+ = R_{N2} + 6.234 + 0.950/t_e([\text{N II}]) - 0.42 \log t_e([\text{N II}]) - 0.027 t_e([\text{N II}]) + \log(1 + 0.116x), \quad (11)$$

and obtain $5.49_{-0.01}^{+0.01}$, $5.98_{-0.05}^{+0.05}$, and $6.31_{-0.23}^{+0.22}$, respectively. For nitrogen, we assume $\frac{\text{N}}{\text{O}} \approx \frac{\text{N}^+}{\text{O}^+}$, which gives good approximation within $< 10\%$ uncertainties (e.g., Nava et al. 2006; Amayo et al. 2021), and obtain $\log (\text{N}/\text{O})_{[\text{N II}]} = -1.04_{-0.23}^{+0.22}$. Using $T_e([\text{S III}])$ instead, we obtain a slightly smaller N/O abundance, $\log (\text{N}/\text{O})_{[\text{S III}]} = -1.09$, but with a smaller error bar. Both measurements are consistent with each other.

For Sulfur, we use ionization correction factor ICF (1.07) calculated with Eq. (20) in Izotov et al. (2006) and obtain $\log (\text{S}/\text{O}) = -1.76_{-0.04}^{+0.04}$.

For Ar, we do not have direct electron temperature measurements. We instead use $T_e([\text{S III}])$ and follow Eq.(11) in Izotov et al. (2006):

$$12 + \log \text{Ar}^{2+}/\text{H}^+ = R_{Ar3} + 6.174 + 0.799/t_e([\text{S III}]) - 0.48 \log t_e([\text{S III}]) - 0.013 t_e([\text{S III}]) + \log(1 + 0.220x), \quad (12)$$

With the ICF calculated for Ar^{2+} ($= 1.10$) using Izotov et al. (2006), we obtain $\log (\text{Ar}/\text{O}) = -2.40_{-0.02}^{+0.02}$. We note that Ar^{3+} abundance is generally smaller than that of Ar^{2+} . As such, we decided to derive the Ar abundance only using Ar^{2+} .

3.5. Inference on Neutral Gas Fraction

Since the $[\text{O I}]$ emission primarily originates due to collisional excitation by thermal electrons, its intensity is a measure of the neutral hydrogen content within the warm ionized regions when the oxygen abundance is known. Using $[\text{O I}](6300)/\text{H}\alpha$ ratio, one could infer the neutral gas fraction therein. We follow the formula in Reynolds et al. (1998):

$$\frac{I_{6300}}{I_{\text{H}\alpha}} = 2.63 \times 10^4 \frac{n(\text{H}^0)}{n(\text{H}^+)} \xi \frac{n(\text{O})}{n(\text{H})} \times \frac{t_e^{1.85}}{(1 + 0.605 t_e^{1.105})} \exp\left(-\frac{2.284}{t_e}\right), \quad (13)$$

where $n(\text{O})/n(\text{H})$ is the gas-phase abundance of oxygen, and $\xi = (1 + r)/(\frac{8}{9} + r)$, where $r = n(\text{H}^0)/n(\text{H}^+)$. By using the oxygen abundance and electron temperature obtained with $[\text{N II}]$, which has among the lowest ionization potential, we find $n(\text{H}^+)/n(\text{H}^0) \sim 250$. Applying $T_e([\text{S III}])$ gives a slightly higher ratio, ~ 300 . The

obtained ratio in either case is much higher than those seen in typical warm ionized components at the Galactic plane ($\ll 100$; Reynolds et al. 1998; Haffner et al. 2009). This likely suggests that our spectrum consists of lines from two ionized regions in MACSJ1149-WR1 i.e. hot and warm. However, this fact should not affect the main analysis of our paper, which concerns the former. For example, by using a typical ratio $n(\text{H}^+)/n(\text{H}^0) = 10$, it is suggested that only $< 5\%$ of the observed $\text{H}\alpha$ flux comes from the warm component. While warm ionized media are typically found diffuse and extended, in our two-dimensional spectrum (Fig. 1) we do not find evidence for that, i.e. the spatial extent of the $[\text{O I}]$ line is not significantly different from those of other lines. Spatially resolved spectroscopy may offer further details.

We note that the measured ratio of the doublets, $[\text{O I}] 6300/[\text{O I}] 6364 \sim 3.5$, confirms that $[\text{O I}]$ emission originates in an optically thin region. Smaller ratios (< 3 i.e. optically-thick case) are only seen in young Supernova remnants, of $\lesssim 1$ yr after the outburst (e.g., Li & McCray 1992; Elmhamdi 2011).

4. HOST GALAXY ANALYSIS

4.1. Spectral Energy Distribution Analysis

We infer the spectral energy distribution (SED) of MACSJ1149-WR1 by using SED fitting code *gsf* (ver1.85; Morishita et al. 2019). We utilize the JWST+HST photometric data for the SED analysis. The detailed procedure is outlined in Morishita et al. (2024).

The SED-based star-formation rate (SFR) is calculated with the rest-frame UV luminosity ($\sim 1600 \text{ \AA}$) using the determined SED model. The UV luminosity is corrected for dust attenuation using the UV continuum slope β_{UV} , which is measured by using the posterior SED, as in Smit et al. (2016):

$$A_{1600} = 4.43 + 1.99 \beta_{\text{UV}} \quad (14)$$

The attenuation corrected UV luminosity is then converted to SFR via the relation in Kennicutt (1998):

$$\text{SFR} [M_{\odot} \text{ yr}^{-1}] = 1.4 \times 10^{-28} L_{\text{UV}} [\text{erg s}^{-1} \text{ Hz}^{-1}]. \quad (15)$$

The estimated SFR is then corrected for the Chabrier IMF, by multiplying a factor of 0.63, which is estimated from *fsps* (e.g., Madau & Dickinson 2014). The measured properties are summarized in Table 2.

4.2. Morphology Analysis

MACSJ1149-WR1 is characterized by compact morphology (Fig. 5). We measure the effective radius of MACSJ1149-WR1 using *galfit*, in the same way

as in Morishita et al. (2023). The derived sizes are $R_e = 2.9$ pixel, or 0.7 kpc in F444W (rest-frame IR), 0.6 kpc in F200W (rest-frame optical), and 0.6 kpc in HST/F606W (rest-frame UV). While the measured size is overall small, it is not significantly off from those of star-forming galaxies at similar redshifts (e.g., van der Wel et al. 2014). Using the stellar mass and SFR estimated from our SED analysis, we find stellar mass surface density of $\Sigma_* \sim 2.6 \times 10^9 M_{\odot} \text{ kpc}^{-2}$ and SFR surface density of $\Sigma_{\text{SFR}} \sim 25 M_{\odot} \text{ yr}^{-1} \text{ kpc}^{-2}$. As a reference, compact star forming galaxy populations known as blue nuggets, typically have $\Sigma_* \gtrsim 10^9 M_{\odot} \text{ kpc}^{-2}$, and as high as $\sim 10^{11} M_{\odot} \text{ kpc}^{-2}$ (e.g., Barro et al. 2017). As such, MACSJ1149-WR1 can be considered as a blue nugget but near the boundary.

MACSJ1149-WR1 is well characterized with a single exponential disk profile in all the filters above, with axis ratio close to ~ 1 . We do not find any disturbed feature or multiple peaks within the central part of the galaxy, nor does it have strong color gradient in F115 – F200W (corresponding to rest-frame Balmer break). However, it has a faint feature extended to the East direction.

5. DISCUSSION

5.1. Enhanced Nitrogen-to-Oxygen Abundance

As shown in Fig. 6, MACSJ1149-WR1 has a mildly enhanced N/O-abundance compared to local galaxies of the similar O/H abundance (e.g., van Zee et al. 1998; Pilyugin et al. 2012; Berg et al. 2020). In a typical star forming galaxy, nitrogen enrichment predominantly originates from intermediate-mass stars. This occurs on longer timescales than that of α elements, which primarily come from core-collapse supernovae. As such, the observed high N/O abundance is inconsistent with the standard model.

In the literature, an enhanced N/O abundance has been seen in several individual galaxies (e.g., Teplitz et al. 2000; Sanders et al. 2023b) and as a systematic offset of galaxy populations on the BTP diagram (e.g., Steidel et al. 2014; Masters et al. 2014). However, its origin often remains inconclusive, as it can be attributed to multiple scenarios, including (i) inflow of pristine gas, lowering O/H abundance but not N/O, (ii) the presence of substantial numbers of rapidly rotating massive stars i.e. WR stars (e.g., Vincenzo et al. 2016; Roy et al. 2021). In our case, we have detected a broad component in the He II 4686 line (Sec. 3.1.2). As such, the observed N/O enhancement in MACSJ1149-WR1 is most likely attributed to the presence of WR stars.

Table 1. Emission line measurements of MACSJ1149-WR1.

Line	IP	Flux	σ	EW ₀
	eV	10^{-19} erg/s/cm ²	km/s	Å
HeII ₄₆₈₆	54.4	39.93 ± 2.25	1347.4 ± 310.5	37.8 ± 6.0
[ArIV] ₄₇₁₁	40.74	< 1.16	—	—
HeI ₄₇₁₄	24.6	3.11 ± 0.96	223.3 ± 126.9	2.4 ± 1.6
[ArIV] ₄₇₄₀	40.74	3.74 ± 1.02	282.0 ± 83.2	2.3 ± 1.5
H β ₄₈₆₁	3.4	174.50 ± 1.83	< 164.3	130.3 ± 1.0
HeI ₄₉₂₂	24.6	< 2.07	—	—
[OIII] ₄₉₅₉₊₅₀₀₇	35.1	1271.14 ± 9.80	< 161.2	228.0 ± 0.7
[OI] ₅₅₇₇	0	< 1.46	—	—
[NII] ₅₇₅₅	14.5	1.12 ± 0.47	< 142.8	1.1 ± 0.3
HeI ₅₈₇₆	24.6	21.34 ± 0.68	142.9 ± 4.4	23.8 ± 0.7
[OI] ₆₃₀₀	0	10.15 ± 0.32	151.9 ± 6.5	14.0 ± 0.5
[SIII] ₆₃₁₂	19.1	3.04 ± 0.38	154.8 ± 27.6	4.1 ± 0.6
[OI] ₆₃₆₄	0	2.89 ± 0.09	151.9 ± 6.5	4.0 ± 0.1
SiII ₆₃₇₃	8.2	1.44 ± 0.41	204.0 ± 42.5	2.1 ± 0.6
[NII] ₆₅₄₈₊₆₅₈₃	14.5	52.52 ± 2.66	150.7 ± 2.2	29.3 ± 0.4
H α ₆₅₆₃	3.4	499.15 ± 3.55	142.7 ± 0.4	750.2 ± 2.3
HeI ₆₆₇₈	24.6	5.33 ± 0.33	128.8 ± 11.2	7.5 ± 0.5
[SII] ₆₇₁₆	10.4	24.90 ± 0.42	137.0 ± 2.8	36.0 ± 0.7
[SII] ₆₇₃₁	10.4	22.23 ± 0.41	133.7 ± 3.0	32.4 ± 0.6
OI ₇₀₀₂	0	< 0.86	—	—
HeI ₇₀₆₅	24.6	8.34 ± 0.41	126.5 ± 6.6	14.5 ± 0.7
[ArIII] ₇₁₃₆	27.6	12.24 ± 0.48	136.9 ± 5.2	22.5 ± 0.8
HeI ₇₂₈₁	24.6	1.52 ± 0.46	172.3 ± 36.0	2.8 ± 0.8
[OII] ₇₃₂₀	13.6	4.91 ± 0.41	111.2 ± 12.6	9.5 ± 0.9
[OII] ₇₃₃₁	13.6	5.04 ± 0.46	149.6 ± 18.9	9.4 ± 1.1
[NiII] ₇₃₇₈	7.6	< 0.80	—	—
[NiII] ₇₄₁₁	7.6	< 0.88	—	—
[ArIII] ₇₇₅₁	27.6	1.72 ± 0.43	< 102.6	3.9 ± 0.7
OI ₇₇₇₄	0	< 1.05	—	—
HeI ₇₈₁₆	24.6	< 1.14	—	—
HeI ₈₂₃₇	54.4	< 0.64	—	—
[SIII] ₉₀₆₉	19.1	—	—	—
Pa γ ₉₂₂₉	1.5	3.76 ± 0.44	175.9 ± 19.0	12.5 ± 1.0
[SIII] ₉₅₃₁	19.1	55.88 ± 0.73	158.0 ± 1.5	203.5 ± 1.7
Pa δ ₁₀₀₄₉	1.5	8.08 ± 0.29	< 133.5	29.7 ± 1.0
HeI ₁₀₈₃₀	24.6	66.32 ± 0.53	155.6 ± 1.1	263.6 ± 1.8
Pa γ ₁₀₉₃₈	1.5	14.04 ± 0.31	123.7 ± 2.5	60.0 ± 1.1
OI ₁₁₂₈₇	0	1.00 ± 0.23	162.7 ± 18.0	5.0 ± 1.2
[FeII] ₁₂₅₆₇	7.9	3.33 ± 0.22	142.9 ± 11.9	18.0 ± 1.7
HeI ₁₂₇₉₀	24.6	1.90 ± 0.39	133.6 ± 16.2	8.8 ± 1.3
Pa β ₁₂₈₁₈	1.5	29.20 ± 0.52	121.1 ± 1.8	135.4 ± 1.8

NOTE— Fluxes are in units of 10^{-19} erg/s/cm². Flux errors are 1σ . 2σ upper limits are quoted for those undetected ($S/N < 2$). Attenuation has been corrected using $A_V = 0.43$. EW₀: Rest-frame equivalent width.

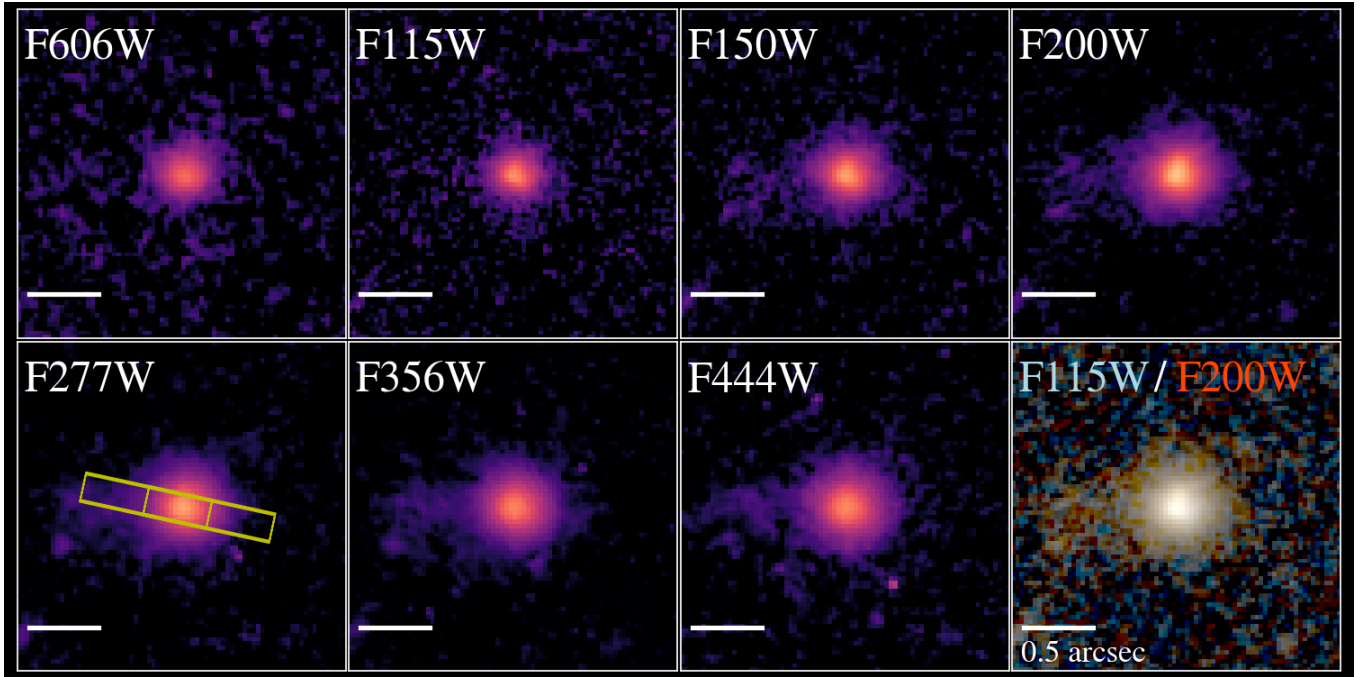


Figure 5. Cutout images of MACSJ1149-WR1 in multiple filters, in the size of $2''.4$ (~ 18 kpc). MACSJ1149-WR1 is characterized by compact morphology across the observed wavelength range. On the F277W stamp, we show the position of our NIRS spec MSA shutters.

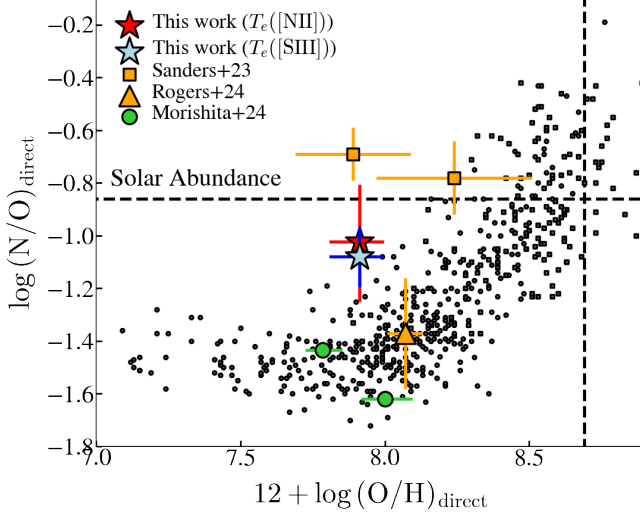


Figure 6. MACSJ1149-WR1 on the $(\text{N/O})_{\text{direct}} - (\text{O/H})_{\text{direct}}$ abundance plane. Also shown are the measurements of H II regions in local galaxies from the CHAOS survey (Berg et al. 2020, black squares) and from Pilyugin et al. (2012, black circles), as well as galaxies at $z \sim 2-3$ from recent observations with JWST by Sanders et al. (2023b, orange squares) and Rogers et al. (2023, triangle), and $z = 3.4$ and 4.3 from Morishita et al. (2024, green circles).

MACSJ1149-WR1 has stellar mass of $\log M_*/M_\odot \sim 9.6$. It is unlikely that this amount of stellar mass was formed through a single, short-term burst event — assuming a constant star formation, at the rate of the inferred SFR (Table 2), it would take > 100 Myr to reach the observed mass, which is much longer than the typical time scale of the WR phase for massive stars i.e. $\lesssim 1$ Myr. As such, it is more plausible to assume that MACSJ1149-WR1 had a star forming phase in the past. In fact, the SFH derived with *gsf* indicates that the $\sim 90\%$ of the observed mass had been formed $\gtrsim 100$ Myr prior to the observed redshift, or at $z > 3$.

It is fair to note that not all high- z galaxies have an enhanced N/O abundance. In Fig. 6, we also show recent measurements of $(\text{N/O})_{\text{direct}}$ with JWST, at $z = 2.96$ (Rogers et al. 2023) and $z = 3.35$ and 4.25 (Morishita et al. 2024). Their N/O abundances are similar to those found in the local galaxies for the corresponding O/H value. As Shapley et al. (2015) noted, the WR scenario may be unlikely for general galaxy populations, due to the timing requirement to capture the very young stage of the galaxy. Investigating the fraction of WR galaxies with a larger sample will help getting such a timescale estimate.

5.2. On the absence of AGN

MACSJ1149-WR1 is characterized by compact morphology. In addition, we detect the $[\text{Fe II}] 1.257$ line,

which is often seen in AGN or shock-ionized regions around O/B-type stars (e.g., Mouri et al. 2000). The presence of AGN could significantly affect the inference of ISM properties, as our analysis implicitly assumes that line emission is primarily driven by photoionization by stellar radiation. At the first glance of the spectrum, the scenario is unlikely, as we do not detect any high ionization lines nor see any broad lines. Here we further investigate this by using multiple emission line diagnostics.

The first is the BPT diagram (Baldwin et al. 1981; Kewley et al. 2006), shown in Fig. 7. MACSJ1149-WR1 is located on the left-top locus of the diagram, near the sequence of local star-forming galaxies. Its location (i.e. high $\text{O3N2} \equiv \log([\text{O III}]/\text{H}\beta) - \log([\text{N II}]/\text{H}\alpha)$) indicates a hard radiation field and a low O/H abundance, commonly seen at similar redshifts (e.g., Strom et al. 2017). A consistent trend is observed in other strong line ratio diagnostics, such as the [O I]-BPT ($[\text{O I}]/\text{H}\alpha - [\text{O III}]/\text{H}\beta$) and the [S II]-BPT ($[\text{S II}]/\text{H}\alpha - [\text{O III}]/\text{H}\beta$).

We note that on the BPT diagram MACSJ1149-WR1 is shifted toward the high $[\text{N II}]/\text{H}\alpha$ ($\sim +0.3$ dex) compared to the local star-forming galaxies of similar $[\text{O III}]/\text{H}\beta$ values. We attribute this to the enhanced N/O abundance as discussed in Sec. 5.1.

In the right panel of Fig. 7, we show the $[\text{Fe II}]/\text{Pa}\beta - [\text{O I}]/\text{H}\alpha$ diagram, which is used to diagnose the presence of shock excitation, as well as to discriminate Seyfert, starburst, and H II region (e.g., Mouri et al. 2000). MACSJ1149-WR1 is located in the middle, consistent with local starburst galaxies. Shock dominated regions seen in supernovae remnants, exhibit a high $[\text{Fe II}]/\text{Pa}\beta$ ratio, > 1 , a factor of ~ 10 higher than the observed value in MACSJ1149-WR1. Izotov & Thuan (2016) also investigated the ratio in local 18 low-metallicity blue compact dwarf galaxies and concluded that shock excitation is not required to explain their observed ratio, $[\text{Fe II}]/\text{H}\beta \lesssim 0.05$ (corresponding to $[\text{Fe II}]/\text{P}\beta \lesssim 0.3$). Recently, Brinchmann (2023) found the same ratio exceeding > 0.5 in three galaxies at $z = 1.2-2.5$, observed with JWST. While their values are consistent with the presence of shock-dominated regions, they noted that further diagnostics would be required.

5.3. He I lines as an independent probe of ISM

We detect multiple He I lines across the observed wavelength range. He I lines are underused in standard ISM analyses, due to their relatively faint nature compared to Hydrogen recombination lines, as well as their complicated aspects coming from collisional excitation and self-absorption. However, the lines could be useful, because (i) the inference via He I is not affected by

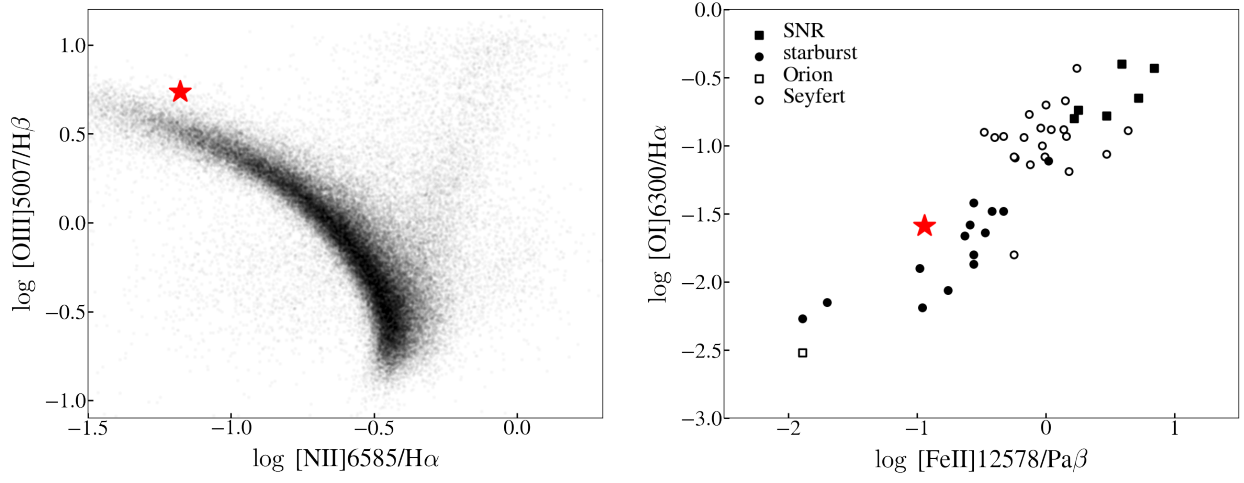


Figure 7. (Left): MACSJ1149-WR1 on the BPT diagram. The location on the diagram indicates that MACSJ1149-WR1 is not classified as AGN but exhibits hard ionization. Local galaxy measurements, taken from JHU-MPA catalog, are shown (black dots). (Right): MACSJ1149-WR1 on the $[\text{Fe II}]/\text{Pa}\beta$ – $[\text{O I}]/\text{H}\alpha$ diagram, along with local supernovae remnant (filled squares), Seyfert (open circles), starburst (filled circles), and H II region (Orion; open square) samples taken from Mouri et al. (2000). The location of MACSJ1149-WR1 on this diagram indicates that shock excitation is not required to explain the observed $[\text{Fe II}]/\text{Pa}\beta$ ratio.

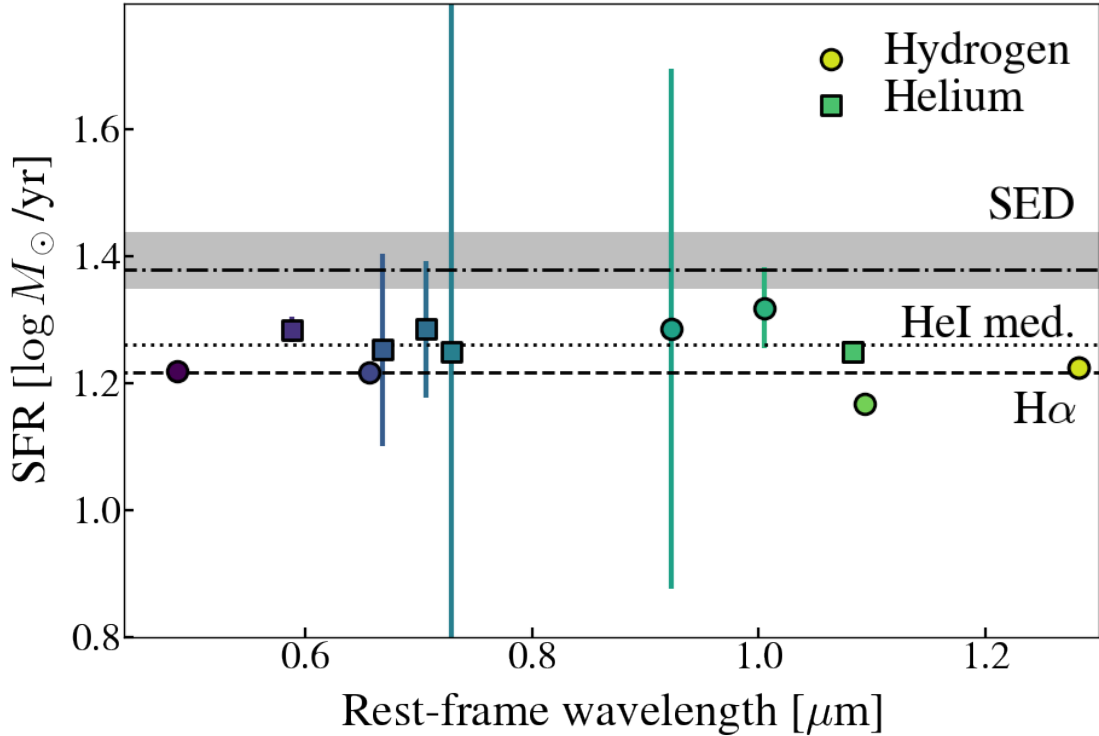


Figure 8. Comparison of SFR measured by using various Hydrogen (circles) and He I recombination lines (squares). The mean (equally weighted) He I SFR is shown (dotted line) for comparison with $\text{H}\alpha$ SFR (dashed line) and SED-based SFR (dash-dotted line). The excellent agreement indicates that He I lines may be used as an independent SFR indicator.

metallicity, (ii) He I has a higher ionization potential (24.6 eV) than H I. As such, they can serve as another independent probe of multi-phase ISM, especially in regions dominated by young stars. Here, we proceed our analysis step-by-step.

We first estimate the electron temperature of He I. The line ratio $I(7281)/I(6678)$ is known as an excellent temperature indicator, with a small dependence on electron density or optical depth (e.g., [Zhang et al. 2005](#)). By using the analytic formulae provided by [Benjamin et al. \(1999\)](#) for the emissivities and $n_e = n_e([\text{S II}])$ (Sec. 3), we find $T_e = 1.7^{+1.3}_{-0.8} \times 10^4 \text{ K}$. Using $I(7281)/I(5876)$, another temperature indicator, we find a similar value, $T_e = 2.0^{+1.0}_{-0.8} \times 10^4 \text{ K}$. The inferred values are higher than those in Sec. 3.4, though the uncertainty is relatively large, due to the lower S/Ns of He I lines.

We then estimate optical depth, τ_{3889} , by using the line ratio $I(7065)/I(7281)$. This is due to self-absorption of the meta-stable triplet, which primarily affects the ortho lines (3889, 4471, 5876, 7065, 10830 Å). While He I 7065 is significantly sensitive to such effect, He I 7281 is almost insensitive ($\Delta I(7281) < 8\%$ up to $\tau \sim 100$; [Benjamin et al. 2002](#)). Using the electron temperature derived above and the same electron density, we obtain the optical depth at rest-frame 3889 Å $\tau_{3889} = 2.8 \pm 0.8$. We then correct He I line fluxes for the optical depth.

Lastly, we derive nebular extinction using the τ -corrected He I fluxes, in the same manner as in Sec. 3.2. Even though the fluxes had been corrected for extinction beforehand using Hydrogen recombination lines in Sec. 3.2, we here find additional extinction of $\Delta \sim 0.1 \text{ mag.}$ indicating that He I may be probing a slightly more attenuated region.

The results above can be explained by the fact that He I has a higher ionization potential, and that the lines predominantly originate in the central region of the galaxy, whereas the H II region is relatively more extended (e.g., [Osterbrock 1989](#)), to the extent where [O I] is more dominant than [O II] and [O III], as revealed in our analysis in Sec. 3.5. Since MACSJ1149-WR1 exhibits compact morphology, more enhanced dust is expected in its central region, where intense massive star formation is likely ongoing, as evidenced by the presence of He II line complex (Sec. 3.1.2).

With the additional ISM diagnostics obtained with He I, we now evaluate its fidelity by comparing star formation rates derived by each of the He I lines with those derived by Hydrogen recombination lines. We note that the conclusion in Sec 5.2 assures that the measured

fluxes of Hydrogen and Helium lines are mostly dominated by recombination i.e. star formation.

We use the He I Case B coefficients used in the analysis above, and the intensity ratio between He I 5867 and H α assuming the Helium abundance of $Y = 0.252$ for the corresponding O/H (e.g., [Izotov et al. 2014](#)), i.e. $n_{\text{He}^+}/n_{\text{H}^+} = 0.0852$, or equivalently $I_{5867}/I_{\text{H}\alpha} = 0.040$. This scaling is roughly consistent with observations of local galaxies. In the Sloan DR7 JHU-MPA catalog, we find the average scaling of $I_{5876}/I_{\text{H}\alpha} \sim 0.033$. The smaller value found with the JHU-MPA catalog is likely due to the fact that the correction for τ_{3889} was not applied to their flux measurements.

In Fig. 8, we show the SFRs derived with various lines and one from the SED analysis in Sec. 4.1. Across the wavelength range, we see an excellent agreement, with SFRs from He I being higher but only $\lesssim 0.1 \text{ dex}$, and the difference is still smaller than the one derived from SED fitting. The agreement seen in Fig. 8 is encouraging, and demonstrates a potential use case of He I lines as an alternative SFR indicator. Especially, at the rest-frame wavelength of $\sim 1.1 \mu\text{m}$, the He I 10830 is among the brightest, and even much brighter than the adjacent Pa γ . (The observed ratio for MACSJ1149-WR1 is $I_{10830}/I_{\text{Pa}\gamma} = 4.8$.) Fig. 9 shows the theoretical predictions for the line intensity normalized by Pa γ and H β . In addition, the line is observable with JWST NIRSpec over a wide range of redshift, $0 \lesssim z \lesssim 4$. With these aspects, we see that future studies may benefit from the line. For convenience, we provide the following formula for the He I 10830–SFR conversion:

$$\text{SFR}/M_{\odot}\text{yr}^{-1} = \left(\frac{C}{0.0852 Y} \right) \left(\frac{L_{\text{He I}, \lambda 10830}}{2 \times 10^{41} \text{ erg s}^{-1}} \right), \quad (16)$$

for the Chabrier IMF, where the conversion coefficient C includes the effect of n_e , T_e , and τ_{3889} . Y is the Helium mass fraction, which in this study we derived with $Y = 0.25 + 26.13 \times 10^{\log(\text{O/H})}$ ([Izotov et al. 2014](#)). We have tabulated the conversion coefficients for various parameters in Table 3.

However, care must be taken. Our analysis involves multiple He I lines, as well as n_e inferred with [S II]. All these have enabled us to robustly obtain T_e , τ , and nebular extinction of He I. The He I 10830 line is meta-stable and subject to self-absorption. For example, the line ratio I_{10830}/I_{5876} can significantly vary as a function of electron density (Fig. 9). Similarly, it has a mild temperature dependence, and the difference can be $\sim 40\%$ between 10000 K and 20000 K.

6. SUMMARY

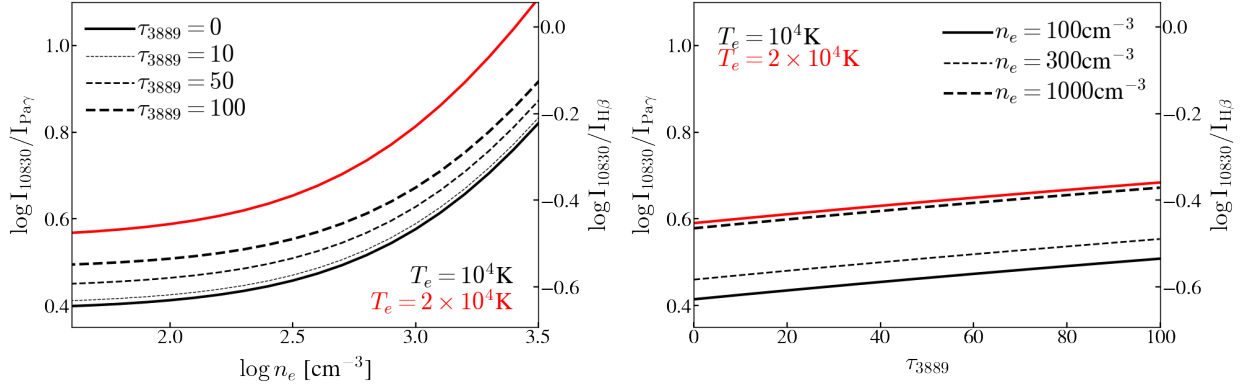


Figure 9. (Left): Theoretical predictions for the line ratio $\text{He I } 10830/\text{Pa}\gamma$ for $T_e = 10^4 \text{ K}$ and various $\text{He I } 3889$ optical depth τ_{3889} , as a function of electron density (n_e ; black lines). The prediction for $T_e = 2 \times 10^4 \text{ K}$ and $\tau_{3889} = 0$ is also shown. (Right): Same ratio is shown but as a function of He I optical depth τ_{3889} for various electron density. The prediction for $T_e = 2 \times 10^4 \text{ K}$ and $n_e = 100 \text{ cm}^{-3}$ is also shown.

We reported JWST/NIRSpec observations of a star-forming galaxy at $z = 2.76$, MACSJ1149-WR1. Our findings are summarized as follows:

- We detected three auroral lines, $[\text{S III}] 6312$, $[\text{O II}] 7320, 7331$, and $[\text{N II}] 5755$. We found that the electron temperatures derived using those lines are consistent.
- MACSJ1149-WR1 exhibits a broad line complex at rest-frame wavelength of $\text{He II } 4686$. Along with the observed high-N/O abundance, we concluded that MACSJ1149-WR1 is a young galaxy that hosts a significant number of Wolf-Rayet stars.
- We diagnosed the presence of AGN by using strong emission lines and concluded that the observed features of MACSJ1149-WR1 is primarily driven by photoionization, validating our ISM analysis.
- We performed another ISM analysis using a series of He I lines, and found that He I is likely probing a smaller scale region than H I . The inferred properties are broadly consistent with the results above.

With the exceptional sensitivity of JWST, we conducted an in-depth analysis of emission lines. Although our study focused on a single galaxy, ongoing JWST observing programs like CECILIA (Strom et al. 2023) and AURORA (Shapley et al. 2021, 2024) will soon allow for the precise examination of ISM properties across a large number of galaxies at similar redshifts. Further exploration of galaxies exhibiting evidence of Wolf-Rayet stars, as discovered in MACSJ1149-WR1, would be of great interest. Determining the prevalence of these fea-

tures across a large number of galaxies will provide critical insights into the timescale of massive star formation and the initial mass function.

In addition, we have demonstrated that He I lines can serve as an independent probe of galaxy ISM. Particularly noteworthy is the strength of the $\text{He I } 10830$ line compared to adjacent $\text{Pa}\gamma$. This line can be as strong as $\text{H}\beta$ under moderate attenuation, $A_V \gtrsim 1 \text{ mag}$. Since this line falls in the wavelength range of the sensitive spectrographs onboard JWST up to $z \sim 4$, we anticipate it becoming another reliable calibrator for star formation rate.

ACKNOWLEDGEMENTS

TM would like to thank Lee Armus and Ranga-Ram Chary for useful discussion. Some/all of the data presented in this paper were obtained from the Mikulski Archive for Space Telescopes (MAST) at the Space Telescope Science Institute. The specific observations analyzed can be accessed via [10.17909/q8cd-2q22](https://archive.stsci.edu/10.17909/q8cd-2q22). We acknowledge support for this work under NASA grant 80NSSC22K1294. SS has received funding from the European Union’s Horizon 2022 research and innovation programme under the Marie Skłodowska-Curie grant agreement No 101105167 - FASTIDIoUS.

Software: Astropy (Astropy Collaboration et al. 2013, 2018, 2022), bbpn (Morishita 2023), EAzy (Brammer et al. 2008), EMCEE (Foreman-Mackey et al. 2013), gsf (Morishita et al. 2019), numpy (Harris et al. 2020), python-fsps (Foreman-Mackey et al. 2014).

Table 2. Physical properties of MACSJ1149-WR1

Property	Unit	Measurement
Host properties		
R.A.	degree	$1.773851e + 02$
Dec.	degree	$2.237533e + 01$
M_*	$\log M_\odot$	$9.6^{+0.2}_{-0.1}$
$A_{V,SED}$	mag	$0.3^{+0.1}_{-0.1}$
β_{UV}		$-1.7^{+0.1}_{-0.1}$
R_e	kpc	$0.7^{+0.1}_{-0.1}$
ISM properties		
$n_e([SII])$	10^2 cm^{-3}	$3.63^{+0.76}_{-0.64}$
$T_e([SIII])$	10^4 K	$1.47^{+0.17}_{-0.14}$
$T_e([NII])$	10^4 K	$1.37^{+0.38}_{-0.25}$
$T_e([OII])_{[OIII]}$	10^4 K	$1.39^{+0.07}_{-0.07}$
$T_e([OIII])_{[NII]}$	10^4 K	$1.47^{+0.45}_{-0.33}$
$T_e([OIII])_{[SIII]}$	10^4 K	$1.50^{+0.19}_{-0.13}$
$T_e([OI])$	10^4 K	< 1.99
$12 + \log(O^+/H^+)$		$7.33^{+0.04}_{-0.04}$
$12 + \log(O^{2+}/H^+)$		$7.78^{+0.10}_{-0.13}$
$12 + \log(O/H)$		$7.91^{+0.08}_{-0.10}$
$\log(S^+/H^+)$		$5.50^{+0.01}_{-0.01}$
$\log(S^{2+}/H^+)$		$5.98^{+0.07}_{-0.07}$
$\log(S/O)$		$-1.75^{+0.06}_{-0.05}$
$\log(N^+/H^+)$		$6.31^{+0.22}_{-0.23}$
$\log(N/O)_{[SIII]}$		$-1.08^{+0.11}_{-0.11}$
$\log(N/O)_{[NII]}$		$-1.02^{+0.22}_{-0.23}$
$\log(\text{Ar}^{2+}/H^+)$		$5.47^{+0.02}_{-0.02}$
$\log(\text{Ar}/O)$		$-2.40^{+0.02}_{-0.02}$
$n(H^+)/n(H^0)$		242
ISM properties (He I)		
$T_e(\text{HeI}, 6678)$	10^4 K	$2.01^{+0.98}_{-0.82}$
$T_e(\text{HeI}, 5876)$	10^4 K	$1.74^{+1.25}_{-0.78}$
τ_{3889}		$2.80^{+0.80}_{-0.70}$
$A_{V,HeI,SMC}$	mag	0.5
Starformation rates		
SFR_{SED}	$\log M_\odot \text{ yr}^{-1}$	$1.33^{+0.03}_{-0.03}$
SFR_{Hb4861}	$\log M_\odot \text{ yr}^{-1}$	1.06 ± 0.01
SFR_{Ha6563}	$\log M_\odot \text{ yr}^{-1}$	1.06 ± 0.01
$\text{SFR}_{Pa99229}$	$\log M_\odot \text{ yr}^{-1}$	1.13 ± 0.41
$\text{SFR}_{Pa10049}$	$\log M_\odot \text{ yr}^{-1}$	1.16 ± 0.06
$\text{SFR}_{Pa10938}$	$\log M_\odot \text{ yr}^{-1}$	1.01 ± 0.02
$\text{SFR}_{Pa12818}$	$\log M_\odot \text{ yr}^{-1}$	1.07 ± 0.01
$\text{SFR}_{HeI5876}$	$\log M_\odot \text{ yr}^{-1}$	1.13 ± 0.02
$\text{SFR}_{HeI6678}$	$\log M_\odot \text{ yr}^{-1}$	1.10 ± 0.15
$\text{SFR}_{HeI7065}$	$\log M_\odot \text{ yr}^{-1}$	1.13 ± 0.11
$\text{SFR}_{HeI7281}$	$\log M_\odot \text{ yr}^{-1}$	1.09 ± 2.47
$\text{SFR}_{HeI10830}$	$\log M_\odot \text{ yr}^{-1}$	1.09 ± 0.01

NOTE— Measurements are corrected for magnification using $\mu = 1.34$ (Sec. 2). Quoted errors are 1σ .

Table 3. The He I 10830–SFR conversion coefficients.

T_e	τ_{3889}	C			
K		$n_e = 100\text{cm}^{-3}$	$n_e = 300\text{cm}^{-3}$	$n_e = 1000\text{cm}^{-3}$	$n_e = 3000\text{cm}^{-3}$
5000	0	1.2437	1.1949	1.0507	0.7818
5000	10	1.2363	1.1878	1.0445	0.7772
5000	100	1.0755	1.0333	0.9086	0.6761
10000	0	1.0384	0.9426	0.7125	0.4198
10000	10	1.0323	0.9370	0.7083	0.4173
10000	100	0.8980	0.8151	0.6161	0.3630
15000	0	0.8779	0.7751	0.5497	0.3003
15000	10	0.8727	0.7705	0.5465	0.2985
15000	100	0.7592	0.6703	0.4754	0.2597
20000	0	0.7659	0.6656	0.4564	0.2404
20000	10	0.7614	0.6617	0.4537	0.2390
20000	100	0.6624	0.5756	0.3947	0.2079

NOTE— $\text{SFR}/M_{\odot}\text{yr}^{-1} = \left(\frac{C}{0.0852Y}\right) \left(\frac{L_{\text{He I}, \lambda 10830}}{2 \times 10^{41} \text{ergs}^{-1}}\right)$. Coefficients for a wider range of parameters can be found at <https://github.com/mtakahiro/Helium>.

REFERENCES

- Allen, D. A., Wright, A. E., & Goss, W. M. 1976, MNRAS, 177, 91, doi: [10.1093/mnras/177.1.91](https://doi.org/10.1093/mnras/177.1.91)
- Amayo, A., Delgado-Inglada, G., & Stasińska, G. 2021, MNRAS, 505, 2361, doi: [10.1093/mnras/stab1467](https://doi.org/10.1093/mnras/stab1467)
- Anglés-Alcázar, D., Faucher-Giguère, C.-A., Kereš, D., et al. 2017, MNRAS, 470, 4698, doi: [10.1093/mnras/stx1517](https://doi.org/10.1093/mnras/stx1517)
- Arellano-Córdova, K. Z., Berg, D. A., Chisholm, J., et al. 2022, ApJL, 940, L23, doi: [10.3847/2041-8213/ac9ab2](https://doi.org/10.3847/2041-8213/ac9ab2)
- Astropy Collaboration, Robitaille, T. P., Tollerud, E. J., et al. 2013, A&A, 558, A33, doi: [10.1051/0004-6361/201322068](https://doi.org/10.1051/0004-6361/201322068)
- Astropy Collaboration, Price-Whelan, A. M., Sipőcz, B. M., et al. 2018, AJ, 156, 123, doi: [10.3847/1538-3881/aabc4f](https://doi.org/10.3847/1538-3881/aabc4f)
- Astropy Collaboration, Price-Whelan, A. M., Lim, P. L., et al. 2022, ApJ, 935, 167, doi: [10.3847/1538-4357/ac7c74](https://doi.org/10.3847/1538-4357/ac7c74)
- Baldwin, J. A., Phillips, M. M., & Terlevich, R. 1981, PASP, 93, 5, doi: [10.1086/130766](https://doi.org/10.1086/130766)
- Barro, G., Faber, S. M., Koo, D. C., et al. 2017, ApJ, 840, 47, doi: [10.3847/1538-4357/aa6b05](https://doi.org/10.3847/1538-4357/aa6b05)
- Benjamin, R. A., Skillman, E. D., & Smits, D. P. 1999, ApJ, 514, 307, doi: [10.1086/306923](https://doi.org/10.1086/306923)
- . 2002, ApJ, 569, 288, doi: [10.1086/339242](https://doi.org/10.1086/339242)
- Berg, D. A., Erb, D. K., Henry, R. B. C., Skillman, E. D., & McQuinn, K. B. W. 2019, ApJ, 874, 93, doi: [10.3847/1538-4357/ab020a](https://doi.org/10.3847/1538-4357/ab020a)
- Berg, D. A., Pogge, R. W., Skillman, E. D., et al. 2020, ApJ, 893, 96, doi: [10.3847/1538-4357/ab7eab](https://doi.org/10.3847/1538-4357/ab7eab)
- Bertin, E., & Arnouts, S. 1996, A&AS, 117, 393
- Brammer, G. B., van Dokkum, P. G., & Coppi, P. 2008, ApJ, 686, 1503, doi: [10.1086/591786](https://doi.org/10.1086/591786)
- Brinchmann, J. 2023, MNRAS, 525, 2087, doi: [10.1093/mnras/stad1704](https://doi.org/10.1093/mnras/stad1704)
- Brinchmann, J., Kunth, D., & Durret, F. 2008, A&A, 485, 657, doi: [10.1051/0004-6361:200809783](https://doi.org/10.1051/0004-6361:200809783)
- Calzetti, D., Armus, L., Bohlin, R. C., et al. 2000, ApJ, 533, 682, doi: [10.1086/308692](https://doi.org/10.1086/308692)
- Chabrier, G. 2003, PASP, 115, 763, doi: [10.1086/376392](https://doi.org/10.1086/376392)
- Curti, M., Maiolino, R., Curtis-Lake, E., et al. 2023, arXiv e-prints, arXiv:2304.08516, doi: [10.48550/arXiv.2304.08516](https://doi.org/10.48550/arXiv.2304.08516)
- Elmhamdi, A. 2011, AcA, 61, 179, doi: [10.48550/arXiv.1109.2318](https://doi.org/10.48550/arXiv.1109.2318)
- Foreman-Mackey, D., Hogg, D. W., Lang, D., & Goodman, J. 2013, PASP, 125, 306, doi: [10.1086/670067](https://doi.org/10.1086/670067)
- Foreman-Mackey, D., Sick, J., & Johnson, B. 2014, doi: [10.5281/zenodo.12157](https://doi.org/10.5281/zenodo.12157)
- Fukugita, M., Ichikawa, T., Gunn, J. E., et al. 1996, AJ, 111, 1748, doi: [10.1086/117915](https://doi.org/10.1086/117915)
- Gburek, T., Siana, B., Alavi, A., et al. 2019, ApJ, 887, 168, doi: [10.3847/1538-4357/ab5713](https://doi.org/10.3847/1538-4357/ab5713)
- Genzel, R., Newman, S., Jones, T., et al. 2011, ApJ, 733, 101, doi: [10.1088/0004-637X/733/2/101](https://doi.org/10.1088/0004-637X/733/2/101)
- Gordon, K. D., Clayton, G. C., Misselt, K. A., Landolt, A. U., & Wolff, M. J. 2003, ApJ, 594, 279, doi: [10.1086/376774](https://doi.org/10.1086/376774)

- Haffner, L. M., Dettmar, R. J., Beckman, J. E., et al. 2009, *Reviews of Modern Physics*, 81, 969, doi: [10.1103/RevModPhys.81.969](https://doi.org/10.1103/RevModPhys.81.969)
- Harris, C. R., Millman, K. J., van der Walt, S. J., et al. 2020, *Nature*, 585, 357, doi: [10.1038/s41586-020-2649-2](https://doi.org/10.1038/s41586-020-2649-2)
- Izotov, Y. I., Stasińska, G., Meynet, G., Guseva, N. G., & Thuan, T. X. 2006, *A&A*, 448, 955, doi: [10.1051/0004-6361:20053763](https://doi.org/10.1051/0004-6361:20053763)
- Izotov, Y. I., & Thuan, T. X. 2016, *MNRAS*, 457, 64, doi: [10.1093/mnras/stv2957](https://doi.org/10.1093/mnras/stv2957)
- Izotov, Y. I., Thuan, T. X., & Guseva, N. G. 2014, *MNRAS*, 445, 778, doi: [10.1093/mnras/stu1771](https://doi.org/10.1093/mnras/stu1771)
- Keenan, F. P., Johnson, C. T., & Kingston, A. E. 1988, *A&A*, 202, 253
- Kennicutt, Robert C., J. 1998, *ARA&A*, 36, 189, doi: [10.1146/annurev.astro.36.1.189](https://doi.org/10.1146/annurev.astro.36.1.189)
- Kewley, L. J., Groves, B., Kauffmann, G., & Heckman, T. 2006, *MNRAS*, 372, 961, doi: [10.1111/j.1365-2966.2006.10859.x](https://doi.org/10.1111/j.1365-2966.2006.10859.x)
- Laseter, I. H., Maseda, M. V., Curti, M., et al. 2023, arXiv e-prints, arXiv:2306.03120, doi: [10.48550/arXiv.2306.03120](https://doi.org/10.48550/arXiv.2306.03120)
- Li, H., & McCray, R. 1992, *ApJ*, 387, 309, doi: [10.1086/171082](https://doi.org/10.1086/171082)
- Lilly, S. J., Carollo, C. M., Pipino, A., Renzini, A., & Peng, Y. 2013, *ApJ*, 772, 119, doi: [10.1088/0004-637X/772/2/119](https://doi.org/10.1088/0004-637X/772/2/119)
- Madau, P., & Dickinson, M. 2014, *ARA&A*, 52, 415, doi: [10.1146/annurev-astro-081811-125615](https://doi.org/10.1146/annurev-astro-081811-125615)
- Masters, D., McCarthy, P., Siana, B., et al. 2014, *ApJ*, 785, 153, doi: [10.1088/0004-637X/785/2/153](https://doi.org/10.1088/0004-637X/785/2/153)
- Morishita, T. 2023, mtakahiro/bbnp: v1.3, v1.3, Zenodo, doi: [10.5281/zenodo.10067906](https://doi.org/10.5281/zenodo.10067906)
- Morishita, T., & Stiavelli, M. 2023, *ApJL*, 946, L35, doi: [10.3847/2041-8213/acbf50](https://doi.org/10.3847/2041-8213/acbf50)
- Morishita, T., Abramson, L. E., Treu, T., et al. 2019, *ApJ*, 877, 141, doi: [10.3847/1538-4357/ab1d53](https://doi.org/10.3847/1538-4357/ab1d53)
- Morishita, T., Roberts-Borsani, G., Treu, T., et al. 2023, *ApJL*, 947, L24, doi: [10.3847/2041-8213/acb99e](https://doi.org/10.3847/2041-8213/acb99e)
- Morishita, T., Stiavelli, M., Grillo, C., et al. 2024, arXiv e-prints, arXiv:2402.14084, doi: [10.48550/arXiv.2402.14084](https://doi.org/10.48550/arXiv.2402.14084)
- Mouri, H., Kawara, K., & Taniguchi, Y. 2000, *ApJ*, 528, 186, doi: [10.1086/308142](https://doi.org/10.1086/308142)
- Nakajima, K., Ouchi, M., Isobe, Y., et al. 2023, arXiv e-prints, arXiv:2301.12825, doi: [10.48550/arXiv.2301.12825](https://doi.org/10.48550/arXiv.2301.12825)
- Nava, A., Casebeer, D., Henry, R. B. C., & Jevremovic, D. 2006, *ApJ*, 645, 1076, doi: [10.1086/504416](https://doi.org/10.1086/504416)
- Oke, J. B., & Gunn, J. E. 1983, *ApJ*, 266, 713, doi: [10.1086/160817](https://doi.org/10.1086/160817)
- Osterbrock, D. E. 1989, *Astrophysics of gaseous nebulae and active galactic nuclei*
- Osterbrock, D. E., & Ferland, G. J. 2006, *Astrophysics of gaseous nebulae and active galactic nuclei*
- Pérez-Montero, E. 2017, *PASP*, 129, 043001, doi: [10.1088/1538-3873/aa5abb](https://doi.org/10.1088/1538-3873/aa5abb)
- Pilyugin, L. S., Vílchez, J. M., Mattsson, L., & Thuan, T. X. 2012, *MNRAS*, 421, 1624, doi: [10.1111/j.1365-2966.2012.20420.x](https://doi.org/10.1111/j.1365-2966.2012.20420.x)
- Proxauf, B., Öttl, S., & Kimeswenger, S. 2014, *A&A*, 561, A10, doi: [10.1051/0004-6361/201322581](https://doi.org/10.1051/0004-6361/201322581)
- Reynolds, R. J., Hausen, N. R., Tufte, S. L., & Haffner, L. M. 1998, *ApJL*, 494, L99, doi: [10.1086/311154](https://doi.org/10.1086/311154)
- Rogers, N. S. J., Strom, A. L., Rudie, G. C., et al. 2023, arXiv e-prints, arXiv:2312.08427, doi: [10.48550/arXiv.2312.08427](https://doi.org/10.48550/arXiv.2312.08427)
- Roy, A., Dopita, M. A., Krumholz, M. R., et al. 2021, *MNRAS*, 502, 4359, doi: [10.1093/mnras/stab376](https://doi.org/10.1093/mnras/stab376)
- Sanders, R. L., Shapley, A. E., Topping, M. W., Reddy, N. A., & Brammer, G. B. 2023a, *ApJ*, 955, 54, doi: [10.3847/1538-4357/acdad](https://doi.org/10.3847/1538-4357/acdad)
- . 2023b, arXiv e-prints, arXiv:2303.08149, doi: [10.48550/arXiv.2303.08149](https://doi.org/10.48550/arXiv.2303.08149)
- Sanders, R. L., Shapley, A. E., Kriek, M., et al. 2016, *ApJL*, 825, L23, doi: [10.3847/2041-8205/825/2/L23](https://doi.org/10.3847/2041-8205/825/2/L23)
- Sanders, R. L., Shapley, A. E., Reddy, N. A., et al. 2020, *MNRAS*, 491, 1427, doi: [10.1093/mnras/stz3032](https://doi.org/10.1093/mnras/stz3032)
- Sanders, R. L., Shapley, A. E., Clarke, L., et al. 2023c, *ApJ*, 943, 75, doi: [10.3847/1538-4357/aca9cc](https://doi.org/10.3847/1538-4357/aca9cc)
- Sargent, W. L. W., & Filippenko, A. V. 1991, *AJ*, 102, 107, doi: [10.1086/115859](https://doi.org/10.1086/115859)
- Schaerer, D., Marques-Chaves, R., Barrufet, L., et al. 2022, *A&A*, 665, L4, doi: [10.1051/0004-6361/202244556](https://doi.org/10.1051/0004-6361/202244556)
- Shapley, A. E., Reddy, N. A., Kriek, M., et al. 2015, *ApJ*, 801, 88, doi: [10.1088/0004-637X/801/2/88](https://doi.org/10.1088/0004-637X/801/2/88)
- Shapley, A. E., Sanders, R., Berg, D., et al. 2021, *The AURORA Survey: First Direct Metallicity Calibrations at High Redshift, JWST Proposal. Cycle 1, ID. #1914*
- Shapley, A. E., Sanders, R. L., Topping, M. W., et al. 2024, arXiv e-prints, arXiv:2407.00157, doi: [10.48550/arXiv.2407.00157](https://doi.org/10.48550/arXiv.2407.00157)
- Shaw, R. A., & Dufour, R. J. 1995, *PASP*, 107, 896, doi: [10.1086/133637](https://doi.org/10.1086/133637)
- Smit, R., Bouwens, R. J., Labbé, I., et al. 2016, *ApJ*, 833, 254, doi: [10.3847/1538-4357/833/2/254](https://doi.org/10.3847/1538-4357/833/2/254)
- Smith, L. F. 1968, *MNRAS*, 141, 317, doi: [10.1093/mnras/141.3.317](https://doi.org/10.1093/mnras/141.3.317)

- Steidel, C. C., Rudie, G. C., Strom, A. L., et al. 2014, *ApJ*, 795, 165, doi: [10.1088/0004-637X/795/2/165](https://doi.org/10.1088/0004-637X/795/2/165)
- Stiavelli, M., Morishita, T., Chiaberge, M., et al. 2023, *ApJL*, 957, L18, doi: [10.3847/2041-8213/ad0159](https://doi.org/10.3847/2041-8213/ad0159)
- Storey, P. J., & Zeppen, C. J. 2000, *MNRAS*, 312, 813, doi: [10.1046/j.1365-8711.2000.03184.x](https://doi.org/10.1046/j.1365-8711.2000.03184.x)
- Strom, A. L., Steidel, C. C., Rudie, G. C., et al. 2017, *ApJ*, 836, 164, doi: [10.3847/1538-4357/836/2/164](https://doi.org/10.3847/1538-4357/836/2/164)
- Strom, A. L., Rudie, G. C., Trainor, R. F., et al. 2023, *ApJL*, 958, L11, doi: [10.3847/2041-8213/ad07dc](https://doi.org/10.3847/2041-8213/ad07dc)
- Tacconi, L. J., Genzel, R., Neri, R., et al. 2010, *Nature*, 463, 781, doi: [10.1038/nature08773](https://doi.org/10.1038/nature08773)
- Teplitz, H. I., McLean, I. S., Becklin, E. E., et al. 2000, *ApJL*, 533, L65, doi: [10.1086/312595](https://doi.org/10.1086/312595)
- van der Hucht, K. A. 2001, *NewAR*, 45, 135, doi: [10.1016/S1387-6473\(00\)00112-3](https://doi.org/10.1016/S1387-6473(00)00112-3)
- van der Wel, A., Franx, M., van Dokkum, P. G., et al. 2014, *ApJ*, 788, 28, doi: [10.1088/0004-637X/788/1/28](https://doi.org/10.1088/0004-637X/788/1/28)
- van Zee, L., Salzer, J. J., Haynes, M. P., O'Donoghue, A. A., & Balonek, T. J. 1998, *AJ*, 116, 2805, doi: [10.1086/300647](https://doi.org/10.1086/300647)
- Vincenzo, F., Belfiore, F., Maiolino, R., Matteucci, F., & Ventura, P. 2016, *MNRAS*, 458, 3466, doi: [10.1093/mnras/stw532](https://doi.org/10.1093/mnras/stw532)
- Zhang, Y., Liu, X. W., Liu, Y., & Rubin, R. H. 2005, *MNRAS*, 358, 457, doi: [10.1111/j.1365-2966.2005.08810.x](https://doi.org/10.1111/j.1365-2966.2005.08810.x)